Emerging Terahertz Integrated Systems in Silicon

Xiang Yi, *Senior Member, IEEE*, Cheng Wang, *Member, IEEE*, Zhi Hu, *Student Member, IEEE*, Jack W. Holloway, *Member, IEEE*, Muhammad Ibrahim Wasiq Khan, *Graduate Student Member, IEEE*, Mohamed I. Ibrahim, *Student Member, IEEE*, Mina Kim, *Graduate Student Member, IEEE*, Georgios C. Dogiamis, *Member, IEEE*, Bradford Perkins, Mehmet Kaynak, Rabia Tugce Yazicigil, *Member, IEEE*, Anantha P. Chandrakasan, *Fellow, IEEE*, and Ruonan Han, *Senior Member, IEEE*

***Abstract*— Silicon-based terahertz (THz) integrated circuits (ICs) have made rapid progress over the past decade. The demonstrated basic component performance, as well as the maturity of design tools and methodologies, have made it possible to build high-complexity THz integrated systems. Such implementations are undoubtedly highly attractive due to their low cost and high integration capability; however, their unique characteristics, both advantageous and disadvantageous, also call for research investigations into unconventional systematic architectures and novel THz applications. In this paper, we review the current status and future trend of silicon-based THz ICs, with the focus on state-of-the-art THz microsystems for emerging sensing and communication applications in the last few years, such as high-resolution imaging, high medium/long-term stability time keeping, high-speed wireline/wireless communications, and miniaturization of RF tags, as well as THz packaging technologies.**

***Index Terms*— Terahertz (THz), integrated circuit (IC), silicon technology, CMOS, SiGe, BiCMOS, THz source, THz communication, THz sensing, transceiver (TRX), radar, imaging, spectroscopy, molecular clock, THz interconnects, high-speed communication, secure communication, overview, review.**

Manuscript received January 16, 2021; revised May 15, 2021; accepted June 3, 2021. Date of publication June 16, 2021; date of current version August 10, 2021. This work was supported in part by the National Science Foundation under Grant CAREER ECCS-1653100, Grant ECCS-1809917, and Grant SpecEES-1824360; in part by the Massachusetts Institute of Technology (MIT) Lincoln Labs under Grant ACC-672; in part by the Office of Naval Research, Naval Research Labs, Singapore-MIT Research Alliance, Intel through the Semiconductor Research Corporation (SRC) under Grant 2017-IN-2752; and in part by the Analog Devices, Texas Instruments, Taiwan Semiconductor Manufacturing Company (TSMC), TDK USA, and Mitsubishi Electric Research Laboratories. This article was recommended by Associate Editor J. Zhao. *(Corresponding author: Ruonan Han.)*

Xiang Yi was with the Department of Electrical Engineering and Computer Science (EECS), MIT, Cambridge, MA 02139 USA. He is now with the School of Microelectronics, South China University of Technology, Guangzhou 510641, China, and also with the Pazhou Laboratory, Guangzhou 510663, China.

Cheng Wang was with the Department of Electrical Engineering and Computer Science (EECS), MIT, Cambridge, MA 02139 USA. He is now with the School of Electronic Science and Engineering, University of Electronic Science and Technology of China, Chengdu 610054, China.

Zhi Hu was with the Department of Electrical Engineering and Computer Science (EECS), MIT, Cambridge, MA 02139 USA. He is now with Apple Inc., Cupertino, CA 95014 USA.

Jack W. Holloway is with the Department of Electrical Engineering and Computer Science (EECS), MIT, Cambridge, MA 02139 USA, and also with Raytheon Technologies, Tewksbury, MA 01876 USA.

Muhammad Ibrahim Wasiq Khan, Mohamed I. Ibrahim, Mina Kim, Anantha P. Chandrakasan, and Ruonan Han are with the Department of Electrical Engineering and Computer Science (EECS), MIT, Cambridge, MA 02139 USA (e-mail: ruonan@mit.edu).

Georgios C. Dogiamis is with the Components Research Team, Intel Corporation, Chandler, AZ 85226 USA.

Bradford Perkins is with the MIT Lincoln Laboratory, Lexington, MA 02421 USA.

Mehmet Kaynak is with the IHP-Leibniz-Institut für Innovative Mikroelektronik, 15236 Frankfurt, Germany.

Rabia Tugce Yazicigil was with the Department of Electrical Engineering and Computer Science (EECS), MIT, Cambridge, MA 02139 USA. He is now with the Department of Electrical and Computer Engineering, Boston University, Boston, MA 02215 USA.

Color versions of one or more figures in this article are available at https://doi.org/10.1109/TCSI.2021.3087604.

Digital Object Identifier 10.1109/TCSI.2021.3087604

I. Introduction

THE research of the "terahertz (THz) gap" between the traditional electronics and photonics regimes, although appearing as a recent research hotspot, dates back to at least one century ago [1], when scholars endeavored to experimentally bridge the "electric waves" and "heat waves". Molecular spectroscopy at the THz frequencies have also been long sought by astronomers to study the composition of solar systems and galaxies [2]. Over the past few decades, non-invasive THz imaging for both security and medical hydration sensing [3], [4] has emerged as probably the most well known application of the THz wave. The fast evolving wireless communication technologies, which move towards wider bandwidth and more directive beams, also draw increasing attentions to ultra-high-speed THz wireless links [5].

Recent research advances have made it more and more evident that integrated circuit (IC) technology is probably the only solution that meets the unique requirements of some practical THz systems. For example, a THz beam-steering active imaging array would require not only dense placement of electronics within the tight, $(\lambda/2)\cdot(\lambda/2)$ array unit area, but also massive connections with baseband control and signal-processing circuitry; all these can only be possible in ICs. The most critical challenge of THz ICs, when comparing to quantum cascade lasers, vacuum tubes, etc., has been the speed and power limits of solid-state devices. That is why III-V high mobility electron transistors (HEMTs) and heterojunction bipolar transistors (HBTs) prevailed in prior THz circuit research, due to their high speed, high gain, and low noise [6], [7]. In 2007, the maximum oscillation frequency $f_{\max}$ of InP exceeded 1 THz [8]. In 2013, the extrapolated

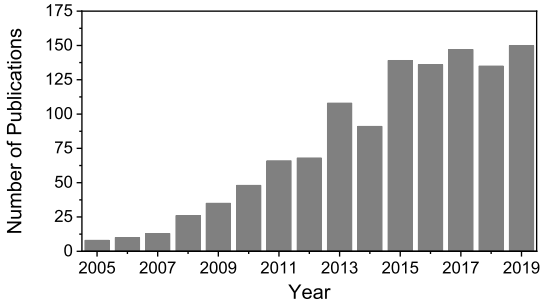

Fig. 1. Number of IEEE publications on silicon-based THz technologies.

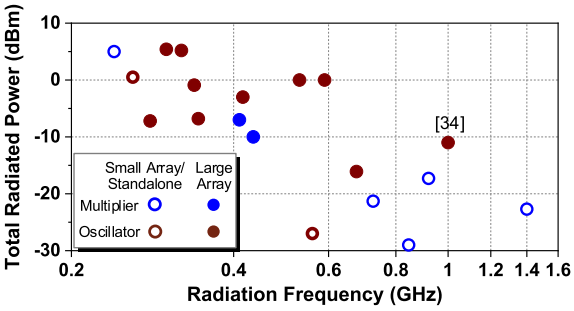

Fig. 2. Total coherent radiated power versus frequency of the works cited in Section II-A.

f_{max} of a 25-nm InP transistor reached 1.5 THz [9], allowing the first 1-THz monolithic amplifier in [9] to achieve 9-dB gain. In [10], a 600-GHz amplifier with >30 dB peak gain using 0.13-μm InP HBT technology is reported. In [11], researchers using 35-nm metamorphic HEMT (mHEMT) technology demonstrated a 610-GHz amplifier with 20.3-dB gain and 6.1-dB noise figure (NF).

Due to the inferior device speed, CMOS and SiGe BiCMOS THz circuits had a later debut with lower demonstrated frequencies. The first >100-GHz and >300-GHz oscillators were presented at International Solid-State Circuits Conference (ISSCC) in 2004 [12] and 2008 [13], [14], respectively. Since then, related research quickly ramps up. Fig. 1 shows the number of IEEE publications[1] on this field, which grows from ~10 in the year of 2005 to ~150 in the year of 2019. That is accompanied by the growth of the f_T and f_{max} of devices, which peak at 300 GHz and 450 GHz respectively for the 22-nm FinFET [15], and 505 GHz and 720 GHz respectively for the 100-nm SiGe HBT [16].

What makes silicon-based THz ICs truly promising, is the low cost and large integration level of prospective THz on-chip systems [17]–[19]. To that end, system chip prototypes started to emerge 5~10 years ago, which mostly aimed at showcasing THz imaging and short-range wireless communication using relatively conventional transceiver (TRX) architectures. Recent years' research efforts have been placing focuses on more practical application scenarios with improved system performance. That urges on re-architecting the CMOS/SiGe systems in order to fully exploit the tight integration of on-chip THz passives, circuits, and other analog/digital circuitry; that in turn enables performance that sometimes could be unprecedented among THz systems using any other technologies. What probably is even more exciting, is that the research community starts to demonstrate new applications (e.g. molecular clock and THz identification or THzID tag) that are completely non-existent in prior THz studies, and only make sense when realized using silicon microelectronics. In this paper, we discuss recent progress of THz signal generation and detection in silicon chips, and then provide an overview of the aforementioned emerging systems and applications for imaging, molecular sensing, time keeping, high-speed communication and ubiquitous tagging. It is worth noting that compared with lower frequency such as millimeter-wave (mm-Wave) solutions, usually THz ICs have wider absolute bandwidth and smaller form factors due to the shorter wavelength, which are demonstrated in our works.

[1]This result is obtained by searching ("THz" OR "terahertz") AND ("CMOS" OR "SiGe") in the publication metadata at IEEE Xplore.

II. Signal Generation and Detection

Given that the wave frequency of a THz circuit in silicon approaches or even exceeds the f_T & f_{max} of the devices, one defining feature of these circuits is the extensive utilization of device nonlinearity and harmonic generation. The resultant degradation of circuit efficiency, although inevitable, can still be minimized through novel circuit topologies as well as the co-design/optimization of circuits with the devices and electromagnetic (EM) passives. In this section, we introduce some recent progress in THz sources and receivers (RXs) using CMOS and SiGe technologies.

A. THz Signal Generation and Radiation

The THz signal generation in a silicon chip is mostly realized via the frequency multiplication of a lower-frequency input signal or an oscillator with the extraction of the high-order harmonic component of the oscillation waveform. A survey on the total radiated power versus frequency of the recent silicon chip works is given in Fig. 2.

By referencing to the input signal, frequency multipliers often offer superior phase noise; they, however, commonly require high input power to ensure optimal conversion rate, which leads to degraded overall energy efficiency. Notable THz multiplier works include [20]–[22] (MOS varactor-based), and [23]–[27] (transistor-based), with output frequencies up to 1.4 THz [21]. The performance comparison between MOS varactor and transistor is highly process dependent and is therefore not conclusive, yet the zero DC power of the varactor-based multiplier surely makes it attractive for efficiency-oriented systems. Compared to nonlinear circuit designs at lower microwave frequencies, which focus mostly on maximizing the nonlinearity of the device quasi-static transfer functions, multiplier designs at THz should also consider the signal loss under various operation conditions, hence often requires a more comprehensive modeling/analysis of the nonlinear device. It also favors compact yet versatile passive structures, which simultaneously create the optimal operation condition for the device and achieve decent input/output matching and signal isolation (i.e. at harmonic frequencies at

the input, and at fundamental frequency at the output) [22], [24]–[26]. Compared to the multipliers, the self-sustaining oscillators with harmonic output often provide higher energy efficiency and much more compact realization. Recent years' research mainly focus on (1) circuit typologies for optimal device oscillation conditions (e.g. the triple push oscillator in [28] and self-feeding oscillator in [29]), (2) holistic EMs design for radiators [30], and (3) versatile circuit structures [31] that combine the functions of (1) & (2). By forming an array of mutually-coupled radiating oscillators [31]–[33], a power-boosting scheme compared to the multipliers is obtained, which quasi-optically combines the THz output of many transistors and delivers higher THz power (Fig. 2). A few mW of total radiated power has been demonstrated in the low-THz regime [31]. One disadvantage of this oscillator scheme is the lack of frequency/phase certainty; that, fortunately, can be fixed with an integrated phase-locked loop (PLL) [31] or injection locking [30].

It is highly attractive to build large-scale 2D active radiator arrays for efficient power combining in free space and for highly directive radiation. The effective isotropically radiated power (EIRP) increases by N^2, where N is the number of elements. However, the scalability of these arrays has always been a challenge, because a high-order harmonic oscillator with built-in antenna is normally much larger than the available $(\lambda/2)\cdot(\lambda/2)$ area, which is set by the requirement of suppressing the sidelobes in the radiation pattern. Such a "half-wavelength dilemma", which is also infamous in the photonics society, severely limits the realizable array size and output power. In [34], a fully "tile · able" 1-THz array is presented to address this issue. A highly versatile slot mesh structure is used, which simultaneously fulfill multiple roles at the fundamental to fourth harmonic frequencies; meanwhile, the physical dimension of the structure is just $(\lambda/2)\cdot(\lambda/2)$ at 1 THz. The array element design, based on a return-current engineering technique that was also previously used in [31], [35]. By manipulating the distribution of the standing wave in the slotlines at different harmonics, the following functions are achieved simultaneously: oscillation at $f_0 = 250$ GHz, suppression of potential radiations at f_0, $2f_0$, and $3f_0$, radiation at $4f_0$, and tight coupling to adjacent elements. The whole array, fabricated using a 0.13-μm SiGe technology, not only allows for a high total radiated power of 80 μW through quasi-optical combining, but also leads to a pencil beam formation. This "tile · able" array technology is applicable for larger array, phase-tunable coupling, frequency tuning, and higher speed/power devices such as InP HBT/HEMT and GaN HEMT. Therefore, the THz source with beam-steering, modulation, and >1 mW radiated power should be feasible which will bring more practical THz applications such as point-to-point wireless communications. More other THz sources works are reviewed in [18], [36], [37].

B. THz Incoherent and Coherent Detection

The first sub-THz square-law detector based on silicon technology was demonstrated based on the Dyakonov-Shur plasma wave detection theory inside a MOSFET[2] [38], [39]. Since then, antenna-integrated MOSFET detector arrays were widely reported with both CMOS bulk and SOI (silicon-on-insulator) technologies [40], [41]. In 2012, [42] reported a 1k-pixel 25-fps real-time THz camera in 65-nm CMOS technology. Meanwhile, Schottky barrier diodes (SBDs) in 130-nm CMOS that use either STI (shallow-trench isolation) or polygate ring as the anode-cathode separation are demonstrated with measured extrapolated f_T of up to 2 THz [43]. Based on these SBDs, a 4×4.280-GHz array and a 860-GHz single channel image sensors were demonstrated [44]. Interestingly, although the above two types of THz detectors are based on completely different devices, the achieved noise equivalent power (NEP), including the antenna loss, is all around tens of pW/Hz$^{1/2}$ at the 0.3∼1-THz regime. There is also no clear performance improvement in more advanced technology nodes, as one may expect. Lastly, a super regenerative detection approach is proposed [45], which reportedly provides sub-pW/Hz$^{1/2}$ NEP at the cost of large detector size and power consumption.

All the above THz components perform essentially phase-incoherent detection. To achieve phase-coherent detection (e.g. for beam forming), a heterodyne down-converter driven by a local oscillator (LO) signal is needed. Compared to the above self-mixing scheme in square-law detectors, mixing the input THz signal with a large-power LO signal also increases the output power and hence the RX sensitivity by orders of magnitude [46]. Since all THz systems to be reviewed next include such a component, more discussions on THz heterodyne RXs will be given later. As an example, the 65-nm CMOS heterodyne RX in the spectrometer of [47] has a measured single-sideband (SSB) NF of 14.6∼19.5 dB across 220∼320 GHz. Note that the core frequency mixing device of almost all silicon THz RXs is a MOS or HBT transistor. In comparison, a recent work in [48] reported an even-order subharmonic mixer using a pair of symmetric MOS varactors [49]. Reactive mixing using varactors, compared to the resistive mixing by transistors, are expected to offer lower loss, lower noise, and higher dynamic cutoff frequency. The measured conversion gain and SSB NF at 550 GHz are -13 dB and 35 dB, respectively.

III. On-Chip Radar and Imaging Systems

Chip-scale radar systems will play a critical role in emerging applications such as manned/unmanned vehicles, industrial robotics, and consumer products. Many of those applications call for significantly increased sensing resolution while keeping the form factor and cost of the radar low. Since better ranging resolution requires larger bandwidth, silicon-based THz radars become very attractive. Conventional frequency-modulated continuous-wave (FMCW) radars are based on a single-channel or single-tone architecture and thus provide limited frequency scanning range due to circuit limitations. A survey of recently reported THz radars in silicon

[2]Since recent years' MOSFET-based detectors exhibit good matching between the standard circuit simulation (which does not model the plasma behavior of the device channel) and measurement, the simpler self-mixing mechanism of the THz signal applied at both the gate and drain of the MOSFET appears to be sufficient to explain and model the detection.

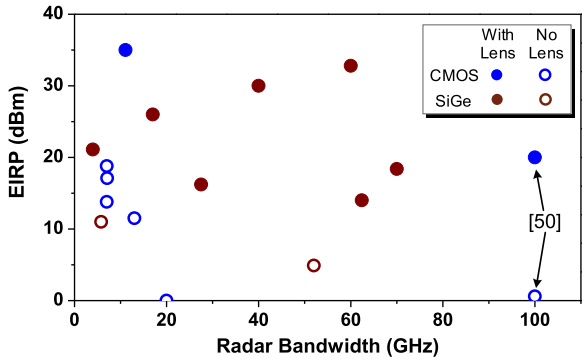

Fig. 3. A survey of prior THz radars using CMOS and SiGe technologies [50].

technologies are given in Fig. 3. At present, the highest reported FMCW bandwidth is 70 GHz from the 130-nm SiGe radar in [52]. With a TPX polymethylpentene lens, excellent EIRP and NF of 18.4 dBm and 19.7 dB are demonstrated, respectively. These values, however, vary by 10.5 dB and 28.6 dB across the 70-GHz bandwidth. Another 55-nm SiGe radar in [53] reduces the EIRP variation to 7.7 dB, but it requires the attachment of a costly silicon lens; compared to [52], the achieved bandwidth and EIRP reduce to 62.4 GHz and 14 dBm, respectively. It is also noteworthy that before 2020, all ultra-broadband radars were based on high-speed SiGe technologies, and the low-cost CMOS-based radars operate below 200 GHz with bandwidths smaller than 20 GHz. In [54], a 2×2 pulse radar array at 160 GHz is built using a 65-nm CMOS technology, and in [55], an FMCW radar at 145 GHz is built using a 28-nm CMOS technology. These CMOS radars deliver bandwidths of 7 GHz and 13 GHz, respectively.

To address the above performance variation and bandwidth limitation problems, a THz-frequency-comb architecture is demonstrated in [51], which adopts a high-parallelism spectral sensing scheme with scalable bandwidth. As a prototype of this approach, a 220-to-320-GHz five-comb-tone radar TRX is implemented using a 65-nm bulk CMOS technology. The block diagram of this radar front-end is shown in Fig. 4a, which includes a daisy chain of successive-frequency-upconversion stages. The SIW (substrate-integrated-waveguide)-backed dual-slot antenna with multiple resonances is adopted to enable both front-side radiation and wide matching bandwidth. As proofed in [51], the downconverted multi-channel intermediate frequency (IF) signals can be stitched together, so this comb radar acts as a wideband radar. The frequency-comb like structure relaxes the circuit and technology requirements for each channel, and the bandwidth requirement for the radar chirping frequency synthesizer. With higher multi-channel-aggregated EIRP, the bandwidth extension is achievable by simply adding more channel TRXs. Fig. 4b, 4c and 4d show the die photo of the 65-nm CMOS chip as well as the packaging including a low-cost TPX lens. With 0.84 W of DC power, the chip itself generates a peak multi-channel-aggregated EIRP of 0.6 dBm, and the fluctuation of the EIRP across the entire 100-GHz bandwidth is only 8.8 dB. With the TPX lens, EIRP is further increased to ~20 dBm. The measured NF has a minimum value of 22.2 dB and a fluctuation of 14.6 dB across the 100-GHz bandwidth. With the IF stitching of five channels, the radar having a bandwidth-limited ranging resolution of 1.5 mm can well resolve the two corner reflectors spaced by 2.5 mm, as shown in Fig. 4e. This is so far the highest reported bandwidth and resolution for FMCW radars. With the recorded 100-GHz bandwidth, it provides the potential applications of high-resolution imaging and detection. In addition, this bandwidth extension technique can be applied to other frequency bands readily.

In addition to the resolution in the longitudinal direction (i.e. ranging resolution), resolution in the azimuth and elevation directions is also desired for the imaging radars to not only "detect" but also "recognize" objects. That is determined by the equivalent antenna aperture size of the radar. Although it favors THz carrier frequencies due to the smaller wavelength and hence small physical size required, achieving fine angular resolution remains highly challenging. Traditional remote sensing equipment utilize synthetic aperture radar (SAR) and inverse synthetic aperture radar (ISAR) to obtain the large aperture through mechanical scan. In [56], an integrated 240-GHz SAR system with 42 GHz of bandwidth is realized with a 120-GHz voltage-controlled oscillator (VCO) that is phase-locked to an external signal. In [53], a compact (0.51 mm^2) 220-GHz FMCW imaging radar using 55-nm SiGe technology is reported, that demonstrates functional ISAR imaging and excellent resolution. Shown in Fig. 5a, the modulated signal in the transmitter (TX) is extracted from the second harmonic of a VCO and is then radiated out through an on-chip slot antenna. At the RX side, the echo signal is received by a folded dipole antenna; it is then downconverted by a sub-harmonic mixer that is driven by the same VCO output as the LO. The radar achieves a wide bandwidth of 62.4 GHz, as well as a lateral resolution better than 2 mm in an ISAR configuration. Impressive 2-D and 3-D images are reconstructed (Fig. 5b and 5c), which shows the feasibility of ISAR imaging with fully-integrated sub-THz imaging systems for security and hydration sensing applications.

One holy grail for THz imagine is a large-scale, heterodyne RX array, which enables large, beam-steering sensing aperture without resorting to mechanical movement. As explained in Section II-B, heterodyne RXs also enable much higher sensitivity than square-law detectors, which can be clearly seen in the survey of Fig. 6. However, due to the same "half-wavelength dilemma" described in Section II-A, building large-scale THz heterodyne RX array has been very challenging. For example, the array element count in [58] and [46] is limited to 4 and 8, respectively, because the centralized phase-locked LO generator requires large chip area and a THz power distribution network that cannot be readily scaled. There is also a trade-off between the number of elements and the LO power available to each heterodyne mixer. To address these issues, in [57], a decentralized 240-GHz 4×8 array architecture is adopted, where the sub-harmonic local oscillator at 120 GHz is incorporated inside each element. The LO phases of all elements are synchronized by coupling neighbour

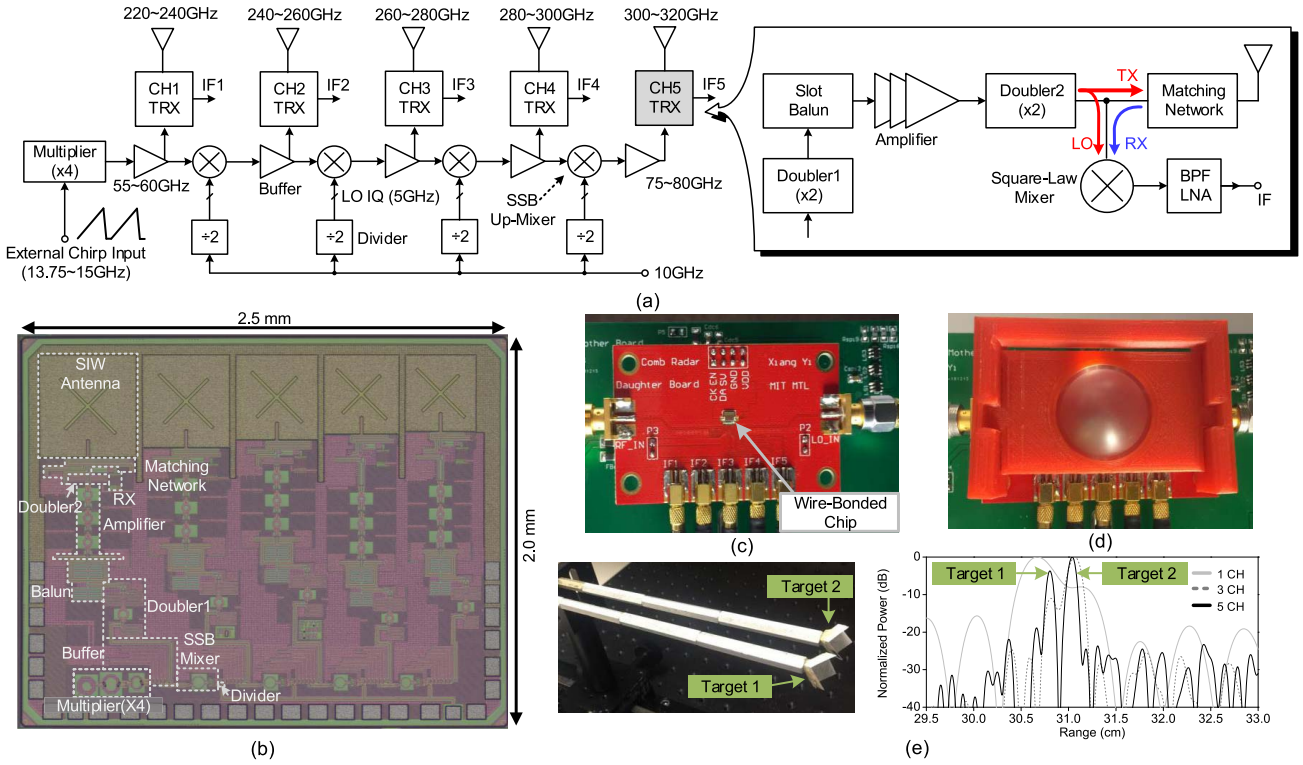

Fig. 4. (a) The block diagram of the 220-to-320-GHz comb radar front-end. (b) Range resolution measurement. (c) Chip micrograph of the comb radar. (d) The wire-bonded chip on a PCB, and (e) the chip package with a front-side TPX lens [51].

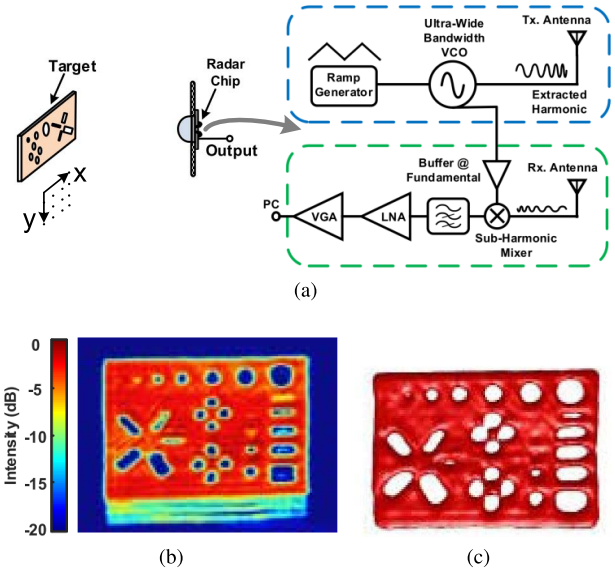

Fig. 5. A 220-GHz ISAR radar developed by researchers at Cornell University, Texas Instruments and University of Michigan: (a) the block diagram of the circuit and the measurement setup; (b) & (c) the measured 2-D and 3-D images of a stencil shape reflector [53].

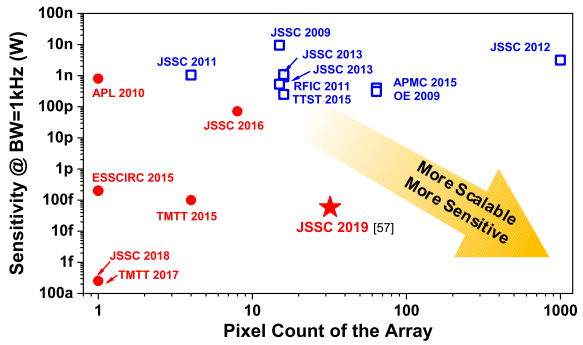

Fig. 6. A comparison between the square-law detector arrays (blue) and heterodyne detector arrays (red) in terms of the integrated pixel count and sensitivity (bandwidth = 1 kHz) [57].

oscillators, and are locked by a 120-GHz PLL. Fabricated in 65-nm CMOS technology, the array element has a measured sensitivity of 58 fW with a detection bandwidth of 1 kHz, which is more than three orders of magnitude better than that of the square-law detector arrays with similar array size. With the extra frequency tuning capacity of each element to cope with the process variation, a very large aperture size becomes feasible, making it attractive for high-resolution beam-forming imaging applications.

Lastly, it is noteworthy that all the above radar and imaging works are based on far-field detection. Such an operation has an ultimate spatial resolution on the level of one wavelength (~mm), which is fundamentally restricted by wave diffraction. For some bio-medicine and material-characterization applications, μm level resolution is required. To break the diffraction limit, a fully-integrated near-field super-resolution 580-GHz sensor is presented in [59], with wave illumination, evanescent-field sensing and 128-pixel detection all integrated on a single 0.13-μm SiGe chip. The detection of each pixel is based on the capacitive interaction between the target material and highly confined E-fields in a split-ring resonator (SRR). Real-time acquisition at 24 fps is demonstrated, and impressive 2-D super-resolution images acquired with a linear scan are

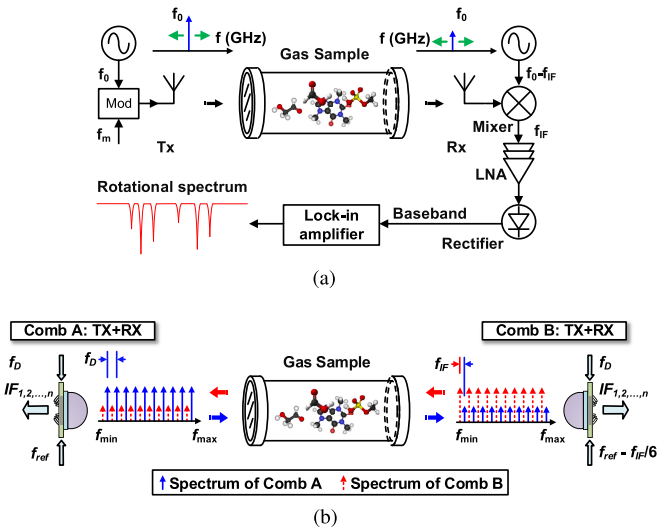

Fig. 7. Rotational spectrometer for molecular analysis: (a) Single-tone spectrometer. (b) Dual-frequency-comb spectrometer [60].

generated. The μm-scale profilometry for imaging objects with a homogeneous permittivity is demonstrated through the image of a human fingerprint. This super-resolution imaging work shows the potential to accelerate the practical THz near-field applications such as medical imaging and security imaging.

IV. Gas Spectroscopy and Time Keeping

THz wave can exert torque onto the electric/magnetic dipole moment of a polar molecule. Transition between quantized rotational energy levels of molecule occurs at certain wave frequencies [61]. Such unique wave-matter interactions have opened up applications that fundamentally distinguish some silicon THz microsystems from their lower-frequency counterparts. In this section, we provide a review for these microsystems.

A. Rotational Spectrometer for Gas Molecular Identification

With a spectrum spanning over hundreds of GHz and a sub-MHz line width (full width at half maximum, FWHM), the rotational spectrum of gaseous molecule is the "fingerprint" of molecular structure [62]. Since overlapping of rotational spectra between two chemical species is highly unlikely, the rotational spectroscopy is capable of identifying an unknown gas mixture with no ambiguity, hence providing so called absolute specificity. Its applications include environmental monitoring, industrial process control, and hazardous agent detection [63]. There are also increasing interests in health monitoring through the analysis of the volatile organic compounds (VOCs) inside human exhaled gas [64]. Many VOCs are bio-markers for clinic diagnosis [65]. For instance, hydrogen sulfide, acetone and toluene have strong correlation with halitosis, diabetes and lung cancer, respectively.

A typical THz rotational spectrometer is shown in Fig. 7a, which adopts a single-tone, frequency-scanning scheme. Based on this scheme, the table-top spectrometer in [66] achieves a state-of-the-art minimum detectable absorption intensity of 2.7×10^{-9} cm^{-1}. To lower the size and cost, CMOS and SiGe single-tone spectrometers have been reported in recent years [67]–[70]. With a 5 mW probing signal at 238∼252 GHz, a 4.3×10^{-6} cm^{-1} minimum detectable absorption intensity has been achieved in [67]. It is noteworthy that the sensitivity of sing-tone spectrometer is capped by the gas saturation threshold [60], which limits the probing signal intensity and thus the achievable signal-to-noise ratio (SNR). Moreover, similar to the single-tone broadband radars in Section III, the power and noise performance of silicon-based spectrometers also degrade significantly with larger bandwidth. Lastly, wideband (e.g. bandwidth = 100 GHz) spectra screening with the required resolution (typically <100 kHz) is a time-consuming procedure (up to a couple of hours). The pulsed echo scheme in [71] is an alternative solution. The 95∼105-GHz spectrometer in [71] adopts a high-Q cavity to enhance the EM field intensity, which reduces the required probing signal power and achieves a 10-kHz level accuracy. However, the mechanical tuning of cavity resonate frequency increases the system complexity and limits the screening speed.

A dual-frequency-comb spectrometer scheme is presented in [47], [60] that leverages the excellent integration capability of CMOS to address the above issues. As shown in Fig. 7b, it uses two 220∼320-GHz comb signals, each with 10 equally-spaced tones, to probe the gas sample with a high-parallelism fashion. The full-band screening time is therefore reduced by 20×. The comb signal is generated by a 65-nm CMOS chip, which has a daisy-chained array of multi-functional, antenna-integrated TRXs. In the measurement, state-of-the-art 5.2-mW total radiated power, 100-GHz-wide comb spectral band, and 14.6∼19.5 dB SSB NF are achieved. For the measured rotational spectra of Carbonyl sulfide (OCS), a 7.2×10^{-7} cm^{-1} minimum detectable absorption has been recorded, which corresponds to a ∼10 ppb minimum detectable concentration with a common pre-concentration gain of 10^3.

B. Chip-Scale Molecular Clock

There is always a strong tie between spectroscopy and accurate time keeping (i.e. building a clock), and THz rotational spectroscopy is no exception. The success of CMOS THz spectrometers makes it possible to innovate a chip-scale "molecular" clock (as an analogy to atomic clocks). This progress is well aligned with some emerging needs in IT infrastructures. The synchronization timing error required by 5G massive multi-input multi-output (MIMO) systems and positioning (with <3 m error) should be below 65 ns [72] and 10 ns [73], respectively. Current 4G long term evolution (LTE) precision timing protocol (PTP), with the assistance of GPS signal only provides μs-level accuracy [74], so new timing infrastructure, including local time holdover devices (i.e. clocks) that are highly-stable (relative error $\leq 10^{-11}$), power-efficient (<0.1 W) and low-cost (<$100). Such clocks are also critical in other GPS-denial applications, such as seismographs for seabed oil exploration [75]. Conventional oven-compensated crystal and micro-electro-mechanical system (MEMS) oscillators, at the expense of high DC power,

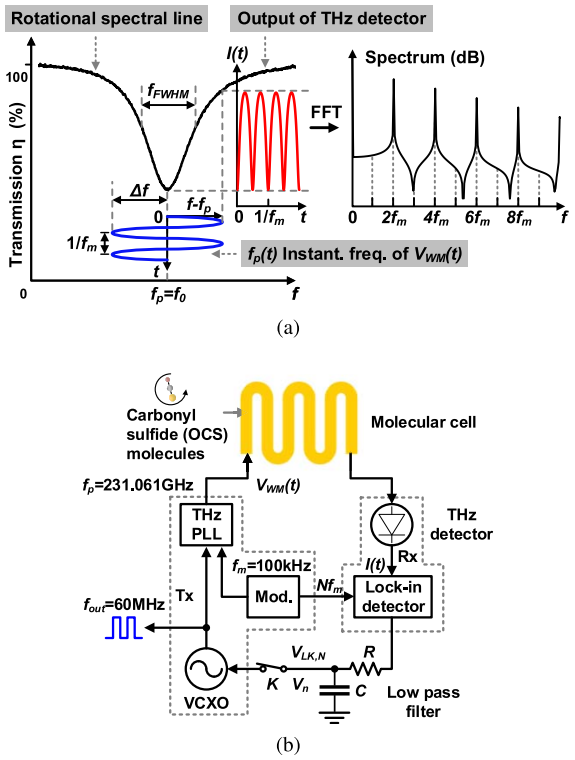

Fig. 8. (a) Wavelength modulation spectroscopy for spectral line probing. (b) Basic schematic of a molecular clock locking to the center of the OCS transition line [82].

provide 10^{-7}∼10^{-8} stability over full temperature range (−20°C to +70°C). Using the coherent population trapping of Cesium or Rubidium atoms in a micro-fabricated vapor cell [76], [77], chip-scale atomic clocks (CSAC) are developed successfully [78]–[80]. The CSAC in [80] delivers stability of $\pm 1 \times 10^{-9}$ within −10°C∼+70°C, while only consuming 60-mW DC power. However, CSACs rely on high-complexity optical-electrical construction, as well as a magnetic-shielded, heated (to 80°C) gas cell with mK temperature-control accuracy, which lead to very high cost and slow start up (3 min in [81]).

THz molecular clock, first introduced in 2018 [83], uses the rotational spectral line of carbonyl sulfide ($^{16}O^{12}C^{32}S$) at $f_0 = 231.061$ GHz as its frequency reference. The selected spectral line has high quality factor (∼10^6) and strong absorption intensity. The transition frequency is also highly stable under temperature variations and external electrical/magnetic fields [84]. Compared with CSACs, the molecular clock is fully electrical and requires no magnetic shield nor heating. The basic locking principle is shown in Fig. 8, where a wavelength-modulated THz signal (with modulation frequency $f_m \approx 100$ kHz) transmits through OCS molecule gas. Due to the gas absorption, the detected envelope of the probing signal, V_{RX}, carries multiple harmonics of f_m. Ideally, when the center frequency f_p of the probing signal aligns with the OCS transition frequency f_0, V_{RX} at odd harmonics of f_m should be zero and can be used as a control signal to dynamically adjust f_p. As is shown in Fig. 8b, the odd harmonic of V_{RX} is extracted through a lock-in amplifier, and the above adjustment is done by controlling a voltage controlled crystal oscillator (VCXO) that serves as the reference of a THz PLL. In the steady state, the MHz-level output of the VCXO is referenced to the stable OCS transition frequency through the PLL division factor, hence is used as the clock output.

What makes the molecular clock highly attractive is the prospective realization of all components other than the gas cell and the crystal oscillator on a single CMOS chip. To demonstrate this vision, two generations of chip-scale molecular clocks have been developed. In [85], a THz CMOS spectroscopic TX/RX chipset is presented, which integrates the electronics in Fig. 8b with a meandered single-mode waveguide gas cell encapsulating OCS molecules. It achieves a measured stability (quantified by Allan deviation) of 3.8×10^{-10} with an averaging time of $\tau = 10^3$ s, while consuming only 66 mW of DC power. A simple frequency-shift-keying (FSK) modulation scheme is adopted to probe the first-order curvature (i.e. $N = 1$ in Fig. 8b) of the OCS transition line. The study on this clock prototype shows that its stability is affected by the non-even transmission baseline of the gas cell, which is estimated to be ∼0.1 dB/GHz [82] and leads to a medium/long-term relative frequency drift of 10^{-9}. To address this issue, a 2^{nd}-generation clock locking to the high odd-order ($N = 3$ in Fig. 8b) curvature of the OCS line is developed [82], as shown in Fig. 11. The high odd-order probing scheme eliminates the above baseline variation problem. It also adopts a cascaded 2-stage PLL structure as well as a new chip-waveguide coupler design (see Section VI for details) to enhance the SNR of the spectroscopic signal. These efforts lead to a measured Allan deviation of 4.3×10^{-11} with an averaging time of $\tau = 10^3$ s, while consuming a slightly higher DC power of 70.4 mW. That further closes the performance gap with CSACs, as is shown in Fig. 9b. Other techniques like lamp dip and packaging techniques can be adopted to fill the performance gap with CSASs.

V. THz Communication Systems

In retrospect, for every 10× increase of data rate, it only takes 7.5 years and 4 years for the wireline and wireless links, respectively [86]. Keeping such momentum, according to Shannon's theorem, inevitably requires broader and broader signal bandwidth. To minimize the spectral congestion and dispersion, THz carrier becomes a natural candidate to support the future >100-Gbps wireless transmission. In ultra-high-speed wireline links, the rapidly-increasing loss and dispersion presented by copper cables to broader baseband signals generates great incentives for the migration to a "wireless-like" transmission scheme through high-frequency waveguides. In this section, we review the state-of-art THz communication systems in silicon, which have been delivering more than 100-Gbps data rate. Meanwhile, we also introduce a special application of THz communication: instead of focusing on the high speed, it aims at promoting the miniaturization and security of wireless chip radios, and hence significantly increasing the ubiquity of, for example, electronic tags.

A. High-Speed Wireline Links Through Guided THz Waves

Rapid increases in data transmission rates and densities within computation and communication infrastructures has

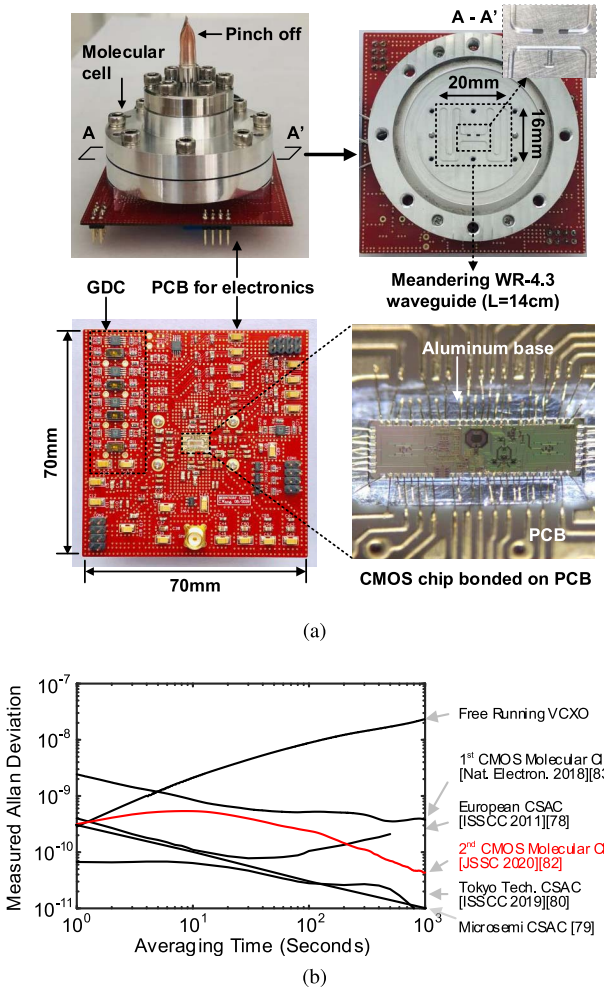

Fig. 9. The 2^{nd}-generation chip-scale molecular clock: (a) CMOS chip and gas cell packaging, (b) measured Allan deviation and comparison with other miniature clocks [82].

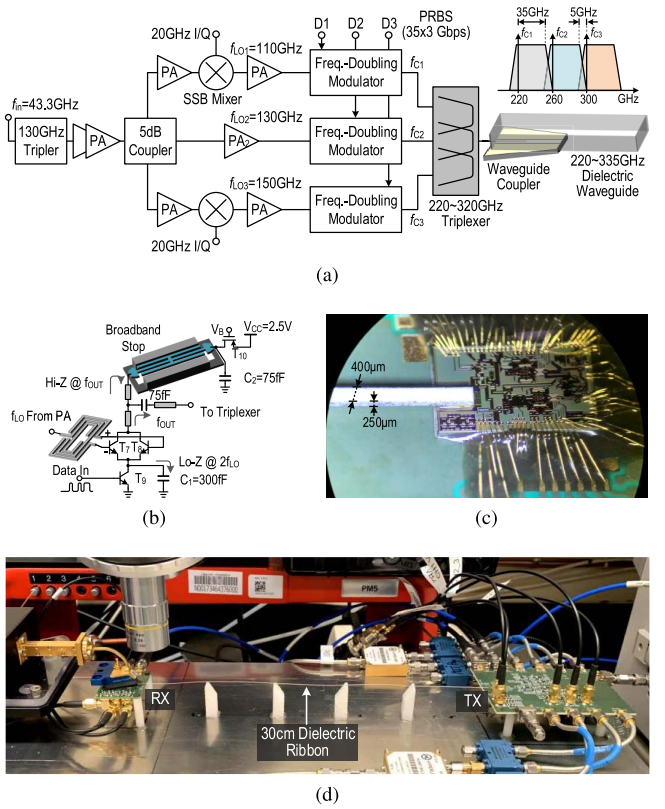

Fig. 10. (a) A 105-Gbps dielectric link: (a) TX architecture; (b) wideband doubler-modulator circuits providing 35-Gbps OOK modulation using a subharmonic LO; (c) photo of the TX chip bonded with a polymer waveguide; (d) setup of the link [87].

led the interconnect community to examine alternatives to conventional copper wireline interconnect for intermediate reach (meter-class). Since 2011 [88], there have been a number of works focused on the use of low-loss dielectric waveguides, carrying modulated data with carriers mostly at D-band (110∼170 GHz) [89]–[92]. Data rate of up to 36 Gbps, meter-level transmission distance and energy efficiency of a few pJ/bit are demonstrated. Moving to the THz operating regime for these types of links is attractive for a number us reasons — namely the higher operating frequencies lend themselves to smaller waveguide cross sections and larger available signaling bandwidths. There are, however, a number of challenges associated with leveraging the inherent advantages of the channel characteristics in the THz regime. Efficient power generation and modulation are still challenging at such frequencies. Furthermore, the wider available signaling bandwidth can be difficult to leverage using wavelength frequency division techniques, due to the poor on-chip passive device quality factor in the THz regime and inefficiency wideband circuit-waveguide coupling structures. The architectural trade offs of these types of links have been examined in [91], [93].

Recently, the first such THz dielectric link incorporating multiple-channel aggregation on an amorphous polymer waveguide is presented in [87]. The TRX chipset is implemented using a 0.13-μm SiGe technology. The architecture of the TX (Fig. 11a) combines three independent signalling channels spanning across the 220 to 335 GHz band via an on-chip hairpin multiplexer and launches the channel-aggregating wave into the polymer waveguide using an integrated coupler. A single-channel RX is used to coherently down-convert and demodulate baseband data at rate up to 35 Gbps for each channel (i.e. overall link rate of 105 Gbps). The carrier signal for each channel is generated by an amplifier-multiplier chain with a shared input at 43.3 GHz. One key component to provide sufficient TX output power with high link efficiency is a combined doubler-modulator output stage shown in Fig. 10b. It is realized based on a current-modulated push-push doubler that is loaded by a broadband, multi-resonance barbell structure. On-off-shift keying (OOK) modulation is provided. By placing each channel's carrier at the lower 3-dB point of each triplexer filter (see Fig. 10a), the lower sideband of the modulated spectrum is suppressed, forming a vestigial sideband transmission. The on-chip waveguide coupler, based on a traveling leaky-wave structure [94], enables efficient (∼5 dB insertion loss) and broadband (bandwidth ≈ 120 GHz) single-mode coupling into and out of a rectangular waveguide that can be directly bonded onto the edge of the chip (see Fig. 10c).

The waveguide is laser cut out of a dielectric sheet ($\epsilon_r \approx 6$). Due to the small wavelength, the cross-sectional dimension of the waveguide is only 0.4 × 0.25 mm^2 (Fig. 10c).

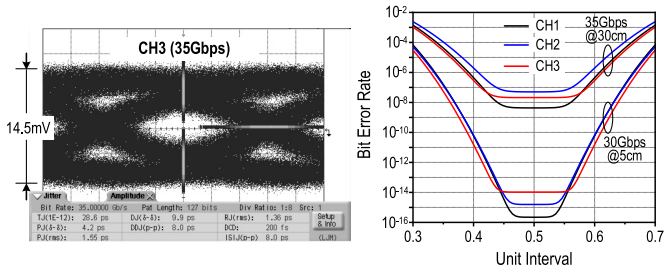

(a)

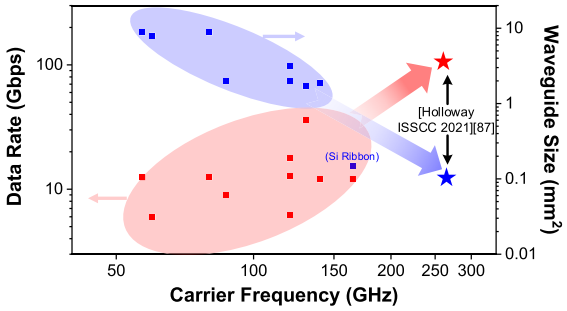

(b)

Fig. 11. (a) Measured eye diagram of Channel 3, while Channel 2 is also transmitting, as well as the bit error rate of the 105-Gbps link. (b) Data rate and waveguide size of dielectric-waveguide links [87].

Fig. 10d shows the link connecting the three-channel TX to a RX using mechanical supports made out of low dielectric-constant polystyrene foam. 3×35 Gbps data rate with 5×10^{-8} bit-error rate (BER) are measured (Fig. 11a). The DC power for the TX chip and the single-channel RX chip is 256 mW and 73 mW, respectively. The overall link energy efficiency is 4.5 pJ/bit. In Fig. 11b, the survey of state-of-the-art dielectric-waveguide links clearly shows the advantages of pushing the carrier frequency towards the THz regime. It is particularly noteworthy that the achieved link data rate density, 332 Gbps/mm, is almost 12 times larger than the prior work [92].

B. High-Speed THz Wireless for Post-5G Communication

Although the "post-5G" wireless protocols are still at their very early stages of development, it is beyond dispute that the data rate will reach an unprecedented level which naturally makes the THz band a strong contender [95]–[99]. Recently, IEEE has established the 802.15.3d WLAN standard, which utilizes the spectrum spanning from 275 to 325 GHz (the so called 300-GHz band) [98]. Targeting at 100-Gbps data rate, it is the first standard of THz band communications toward the post-5G era.

Remarkable progress has been made recently on the high-speed THz wireless TRXs, and the CMOS and SiGe circuit technologies have been playing a critical role. A survey of the achieved data rate and communication distance is provided in Fig. 12. Up to 100-Gbps data rate has been reported. Although the generally small antenna size and lower circuit performance (compared to the <100-GHz counterparts) limit the distance, links operable across up to 1 m are still realized with SiGe processes, mostly due to the higher output power

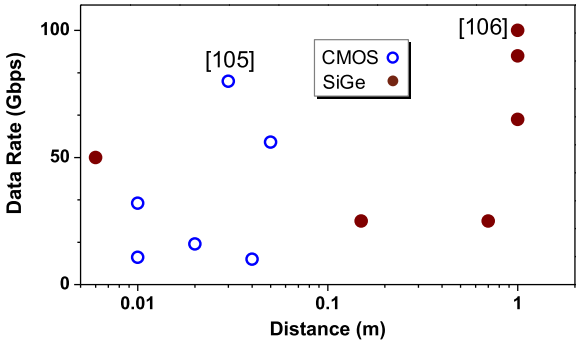

Fig. 12. Survey of high-speed THz wireless communication chips based on silicon technologies.

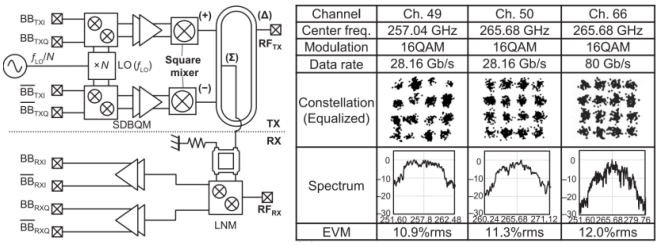

(a)

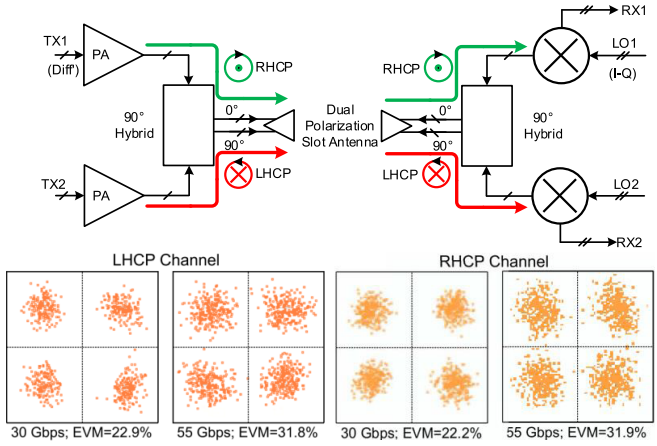

(b)

Fig. 13. (a) Schematic, measured constellations and power spectra of a 300-GHz-band single channel TRX by Hiroshima University [105]. (b) Schematic and measured constellations of a 255-GHz MIMO TRX by University of Wuppertal [106].

than the CMOS circuits. Simple modulation schemes such as OOK are adopted in early THz TRXs [100], [101]. Later, more complex schemes, such as BPSK, QPSK and 16-QAM, are implemented to deliver higher data rate and spectral efficiency [52], [102]–[105]. In [105], a 300-GHz-band single-chip CMOS QAM TRX is presented (Fig. 13a). A novel square mixer design is adopted by the authors, which realizes THz signal generation and modulation simultaneously. The 40-nm CMOS chip consumes DC power of 890 and 897 mW, respectively, in the TX and RX modes. With 16-QAM modulation (Fig. 13a), transmission of 80 Gbps over 3 cm is demonstrated.

Spatial/polarization orthogonality, as well as channel bonding, are extensively exploited to push for higher performance. In [106], the spectral efficiency of a 220-255-GHz, 0.13-μm

SiGe QPSK TRX is doubled by transmitting two 55-Gbps data streams on a left-handed circular polarized (LHCP) wave and a right-handed circular polarized (RHCP) wave (Fig. 13b). A unique antenna system consisting of a dual-polarzation slot antenna and a 90° hybrid enables the superposition and radiation of the above two waves sharing the same frequency. In a 2-stream MIMO measurement, the chip, with 2.85-W DC power, delivers a maximum aggregate data rate of 110 Gbps with an error vector magnitude (EVM) of 31% with 1-m transmission distance (Fig. 13b).

C. THz Backscatter Communication for Ubiquitous ID Tags

THz communication is often conceived as operation with high power consumption and high data throughput. One interesting and important property enabled by THz electronics, which is somehow overlooked in the past, is the unprecedented miniaturization of the radio frequency (RF) system as a whole. That property is critical for RF identification (RFID) tags that are widely adopted in tracking, authentication, supply-chain management and so on [108]. At present, commercial RFID chips rely on external antenna or inductor packaging to facilitate efficient far-field or near-field coupling. That, however, significantly increases the overall size and cost of the tag, making it impossible to be directly attached to objects such as medical pills, tooth implants and semiconductor chips. In order to enable secure and ubiquitous asset tagging, fully-passive, cryptographic "chip particles" without any external packaging are highly desired. Such requirement calls for an aggressive increase of the RFID communication frequency to the THz regime, so that sub-millimeter-sized on-chip antennas can be used.

Recently, an ultra-small (1.2×1.3 mm^2) package-less, monolithic ID tag operating at 260 GHz (hence the name "THzID") is demonstrated using TSMC 65-nm CMOS technology [107], [109]. Fig. 14a shows the size comparison of the THzID with a conventional RFID and one dollar coin. The ultra-high downlink/uplink carrier frequency, along with a TX-RX antenna sharing technique, allow for an on-chip integration of a 2×2 antenna array and a tag-side beam-steering capability for the first time for RF tags. An operation range of 5 cm is demonstrated, which makes barcode-reader-like applications possible. Meanwhile, an ultra-low-power elliptic-curve-cryptography (ECC) dedicated processor is integrated in the THzID chip, which provides high-security and compact asymmetric encryption. The architecture of the tag chip is shown in Fig. 14b. The incident 260-GHz wave (red in Fig. 14b) from the reader is coupled to a 2×2 array of on-chip multi-functional patch antennas. The linearly polarized THz signal, received by each antenna, is extracted from two sets of antenna feeds. Half of the power is used for the downlink based on four square-law detectors. The other half is used for backscatter uplink communication. The backscatter signal is frequency-shifted and radiated with an orthogonal polarization (blue in Fig. 14b). This cross-polarization scheme suppresses the strong, direct-reflection of the reader signal and also allows for the reuse of the antennas. The downlink and uplink, both using OOK modulation, offer data

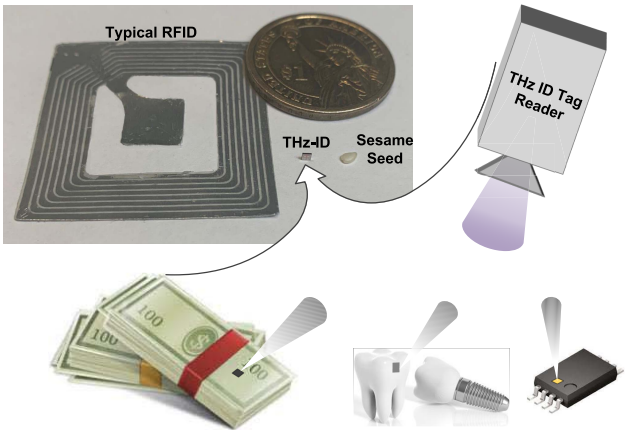

(a)

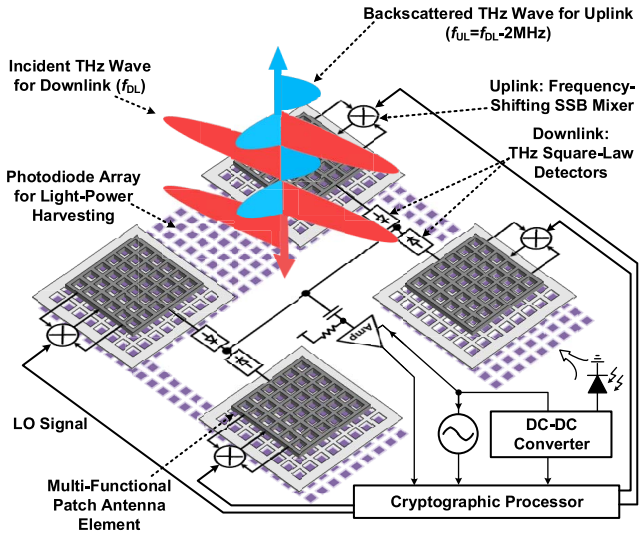

(b)

Fig. 14. (a) Cryptographic THzID tag: size comparison with RFID antenna and $1 coin and its potential applications. (b) Overall architecture of the THzID tag [107].

rates of 100 kbps and 2 kbps, respectively. The integrated ECC security processor based on a narrow-strong private identification protocol [110] under a public-key cryptography scheme ensures that an eavesdropper cannot identify which tag participates in the protocol by merely monitoring the wireless link. The THzID consumes a peak power of 21 μW. Such power can be generated by a built-in array of P-N photodiodes, which is placed under and besides the antennas (Fig. 14b). With ultra-small size and cost, this THz security ID tag has potential applications in manufacturing, logistics, anti-counterfeiting, and so on (Fig. 14a).

VI. Packaging Technologies for Silicon-Based THz Systems

The increasingly significant distributed effect, signal loss, and parasitics that are hard to model pose great challenges to the packaging of THz microsystems [111]. Many emerging THz applications also bring about very unique packaging specifications; for example, the gas-cell package of the chip-scale molecular clock in Section IV not only requires

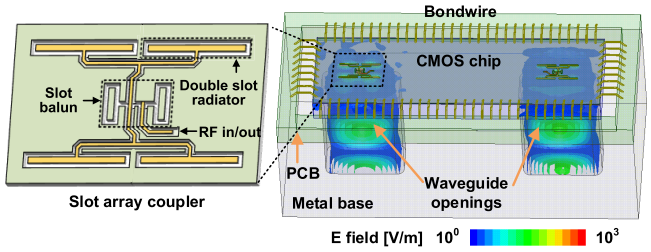

Fig. 15. The chip-integrated rectangular waveguide coupler used in the THz molecular clock in [82].

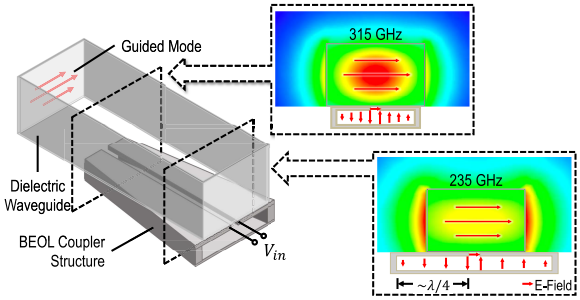

Fig. 16. Wideband planar THz waveguide coupler [94].

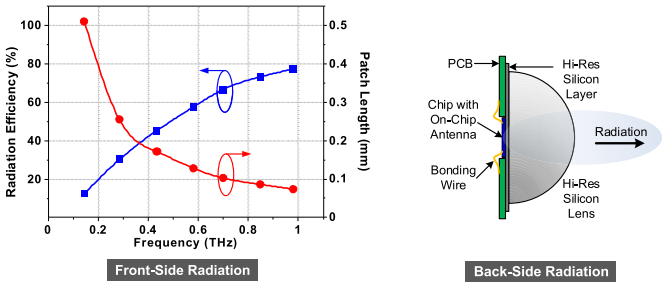

Fig. 17. (a) Front-side radiation with on-chip patch antenna and the simulated radiation efficiency [114]. (b) Back-side radiation with an external hemispheric silicon lens [29].

low THz transmission loss, but also long-term vacuum sealing. A complete discussion about that topic is beyond what this section can cover. Instead, here some techniques that can be applicable to common THz silicon platforms are presented.

Broadband coupling from a silicon chip to an external THz waveguide is often needed. At low frequency, this is normally realized through the wire-bonding to an external waveguide feed structure. However, the parasitic inductance of a bond wire is ~1 nH/mm [112], which largely impedes the THz signal flow. A three-bond-wire configuration forming a G-S-G transmission line can in principle still work; however, the length tolerance may severely degrade the performance [85]. In the InP amplifier work in [113], a chip-integrated dipole antenna demonstrates excellent coupling and should be applicable to silicon chips, too. That, however, requires substrate thinning to tens of μm and placement of the chip inside the waveguide, which limits the chip size and other aspects of the package. In [82], a chip-integrated, 2×2 slot array structure is presented, which radiates the THz wave through the silicon substrate, and then into a WR-3 metal waveguide opening attached at the backside of the chip. The design delivers ~5 dB insertion loss, 21% fractional 3-dB bandwidth, and greatly simplifies the complexity of the package. With high-resistivity substrate such as those in the CMOS SOI processes, the simulated insertion loss is further reduced. In the THz wireline systems discussed in Section V, broadband coupling to a dielectric waveguide is crucial. In [88]–[92], off-chip waveguide launchers with wire-bonding to the chips are used at D-band. For waveguide coupling at even higher frequency, direct integration of the launcher structure has been explored. In [94], a traveling leaky wave launcher based on a SIW structure is innovated (see Fig. 16). With a differential input, the excited EH_1 hybrid mode enables effective coupling between launcher and the waveguide ribbon. Meanwhile, the launcher width is tapered along its longitudinal axis, so that various frequency components are coupled at different sections of the launcher (Fig. 16). An insertion loss of 2.5~6 dB is enabled across a broad, 220~340-GHz band. This technique is also adopted in the 105-Gbps link demonstration [87] described in Section V.

Many THz systems utilize free-space radiation of the wave, so antenna is a critical part of the THz package. While off-chip antennas have been realized at D-band with bond wire [117] or BGA (ball-grid array) package pattern [118]. Antennas operating in the THz regime currently are still implemented on chip. Such a solution, however, has been limited by the presence of the silicon substrate and the close proximity among the metal layers. Patch antenna with ground shield eliminates the impact from the former, but as Fig. 17a shows, the achieved radiation efficiency in the 0.2~0.3-THz range is low. The input matching bandwidth is also lower than 10%. Using slot or dipole antenna coupled with a hemispheric or hyper-hemispheric silicon lens on the chip back (Fig. 17b) effectively increases the efficiency (to ~50%) and the bandwidth [29], [34], [42], [47]. Normally a high-resistivity silicon layer is inserted between the chip and the lens, so as to provide a mechanical support to the chip. The major drawbacks of this approach include the high cost of the lens, complex assembly, and the inferior thermal release. Large antenna array, especially those consisting of different antenna frequencies [47], also requires large lens diameter to avoid beam tilting. Fortunately, Fig. 17a shows that at half-THz and above, patch antenna offers decent efficiency since the metal layer distance, when normalized by the wavelength, is larger. To increase the bandwidth of the front-side radiation antenna, a SIW-backed dual-slot antenna with multiple resonances has been presented [51], with 17% fractional bandwidth.

It is also noteworthy that the chip packaging process can also be used to fabricate high-performance THz components, which, if implemented on chip, often occupy large chip area and are limited by the BEOL layer thickness and spacing. In [116], an RF chip packaging technology is developed, featuring ultra-thick metal layers, lithographic continuous vias and organic build-up dielectric substrate. It enables the high-precision and large-volume fabrication of THz passives (Fig. 18a). For example, an 8-pole channelizer using coupled high-Q SIW cavities is demonstrated in [115], which

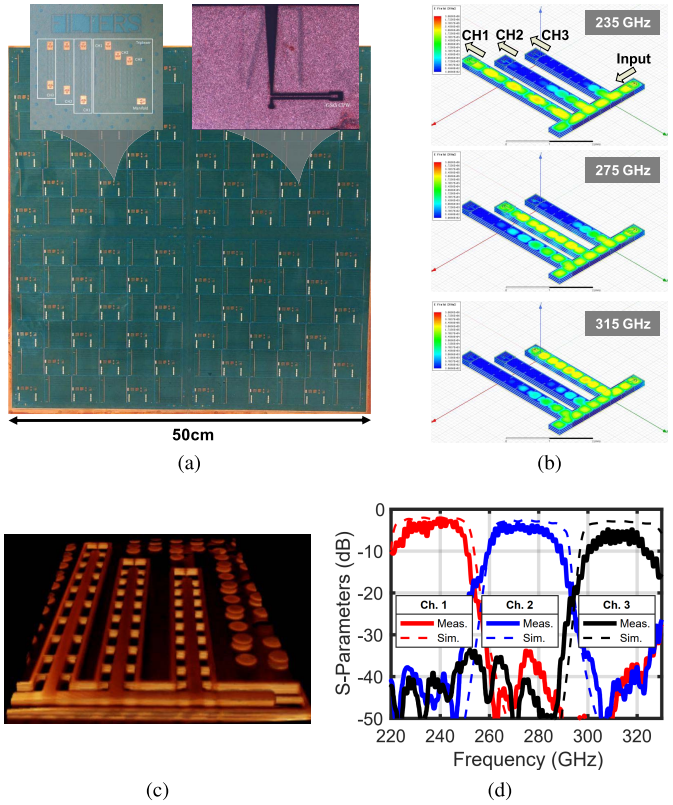

Fig. 18. High-performance THz passive components using organic chip-packaging process: (a) a 0.5 × 0.5-m^2 panel with 220∼340-GHz channelizer and waveguide launcher structures; (b) Simulated E-field distribution in the channelizer at three channel frequencies; (c) a 3D X-ray image of the channelizer, showing the continuous via technology; (d) measured channelizer response [115], [116].

delivers state-of-the-art fractional bandwidth (∼40%) among THz multiplexers.

VII. Conclusion

The development of advanced silicon technologies has enabled the booming of THz circuits and systems. With the ever-increasing performance and integration, novel while practical applications are emerging. Recent demonstrations include imaging with mm far-field resolution and μm near-field resolution, wideband gas spectroscopy with absolute specificity, time-keeping with 10^{-11} level stability, >100-Gbps communications in both wireline and wireless configurations, ultra-small THzID for ubiquitous tagging, and so on. With the continued innovations across the device, circuit and packaging levels, there is no doubt that the application space of future THz microsystems in silicon will be greatly expanded.

References

[1] E. F. Nichols and J. D. Tear, "Short electric waves," *Phys. Rev.*, vol. 21, no. 6, pp. 587–610, Jun. 1923.
[2] C. Kulesa, "Terahertz spectroscopy for astronomy: From comets to cosmology," *IEEE Trans. THz Sci. Technol.*, vol. 1, no. 1, pp. 232–240, Sep. 2011.
[3] K. B. Cooper, R. J. Dengler, N. Llombart, B. Thomas, G. Chattopadhyay, and P. H. Siegel, "THz imaging radar for standoff personnel screening," *IEEE Trans. THz Sci. Technol.*, vol. 1, no. 1, pp. 169–182, Sep. 2011.
[4] Z. D. Taylor *et al.*, "THz medical imaging: *In vivo* hydration sensing," *IEEE Trans. THz Sci. Technol.*, vol. 1, no. 1, pp. 201–219, Sep. 2011.
[5] T. Nagatsuma, "Terahertz communications: Past, present and future," in *Proc. 40th Int. Conf. Infr., Millim., THz waves (IRMMW-THz)*, Aug. 2015, pp. 1–2.
[6] M. Božanić and S. Sinha, "Emerging transistor technologies capable of terahertz amplification: A way to re-engineer terahertz radar sensors," *Sensors*, vol. 19, no. 11, p. 2454, May 2019.
[7] M. Urteaga, Z. Griffith, M. Seo, J. Hacker, and M. J. W. Rodwell, "InP HBT technologies for THz integrated circuits," *Proc. IEEE*, vol. 105, no. 6, pp. 1051–1067, Jun. 2017.
[8] R. Lai *et al.*, "Sub 50 nm InP HEMT device with F_{max} greater than 1 THz," in *IEDM Tech. Dig.*, Dec. 2007, pp. 609–611.
[9] X. Mei *et al.*, "First demonstration of amplification at 1 THz using 25-nm InP high electron mobility transistor process," *IEEE Electron Device Lett.*, vol. 36, no. 4, pp. 327–329, Apr. 2015.
[10] M. Seo *et al.*, "A 600 GHz InP HBT amplifier using cross-coupled feedback stabilization and dual-differential power combining," in *IEEE MTT-S Int. Microw. Symp. Dig.*, Jun. 2013, pp. 3–5.
[11] A. Leuther, A. Tessmann, M. Dammann, H. Massler, M. Schlechtweg, and O. Ambacher, "35 nm mHEMT technology for THz and ultra low noise applications," in *Proc. Int. Conf. Indium Phosph. Rel. Mater. (IPRM)*, May 2013, pp. 1–2.
[12] L. M. Franca-Neto, R. E. Bishop, and B. A. Bloechel, "64 GHz and 100 GHz VCOs in 90 nm CMOS using optimum pumping method," in *IEEE Int. Solid-State Circuits Conf. (ISSCC) Dig. Tech. Papers*, Feb. 2004, pp. 444–445.
[13] E. Seok *et al.*, "A 410 GHz CMOS push-push oscillator with an on-chip patch antenna," in *IEEE Int. Solid-State Circuits Conf. (ISSCC) Dig. Tech. Papers*, Feb. 2008, pp. 472–629.
[14] D. Huang, T. R. LaRocca, L. Samoska, A. Fung, and M.-C.-F. Chang, "324 GHz CMOS frequency generator using linear superposition technique," in *IEEE Int. Solid-State Circuits Conf. (ISSCC) Dig. Tech. Papers*, Feb. 2008, pp. 476–477.
[15] H.-J. Lee *et al.*, "Intel 22 nm FinFET (22FFL) process technology for RF and mm wave applications and circuit design optimization for FinFET technology," in *IEDM Tech. Dig.*, Dec. 2018, pp. 316–319.
[16] B. Heinemann *et al.*, "SiGe HBT with f_x/f_{max} of 505 GHz/720 GHz," in *IEDM Tech. Dig.*, Dec. 2016, pp. 51–54.
[17] R. Han *et al.*, "Filling the gap: Silicon terahertz integrated circuits offer our best bet," *IEEE Microw. Mag.*, vol. 20, no. 4, pp. 80–93, Apr. 2019.
[18] S. M. H. Naghavi, M. T. Taba, R. Han, M. A. Aseeri, A. Cathelin, and E. Afshari, "Filling the gap with sand: When CMOS reaches THz," *IEEE Solid State Circuits Mag.*, vol. 11, no. 3, pp. 33–42, Summer 2019.
[19] K. O. Kenneth *et al.*, "Opening terahertz for everyday applications," *IEEE Commun. Mag.*, vol. 57, no. 8, pp. 70–76, Aug. 2019.
[20] Z. Ahmad and K. O. Kenneth, "0.65–0.73 THz quintupler with an on-chip antenna in 65-nm CMOS," in *IEEE Symp. VLSI Circuits, Dig. Tech. Papers*, Kyoto, Japan, Jun. 2015, pp. C310–C311.
[21] Z. Ahmad, M. Lee, and K. O. Kenneth, "1.4 THz, −13dBm-EIRP frequency multiplier chain using symmetric- and asymmetric-CV varactors in 65 nm CMOS," in *IEEE Int. Solid-State Circuits Conf. (ISSCC) Dig. Tech. Papers*, Jan. 2016, pp. 350–351.
[22] R. Han and E. Afshari, "A high-power broadband passive terahertz frequency doubler in CMOS," *IEEE Trans. Microw. Theory Techn.*, vol. 61, no. 3, pp. 1150–1160, Mar. 2013.
[23] H. Aghasi, A. Cathelin, and E. Afshari, "A 0.92-THz SiGe power radiator based on a nonlinear theory for harmonic generation," *IEEE J. Solid-State Circuits*, vol. 52, no. 2, pp. 406–422, Feb. 2017.
[24] F. Golcuk, O. D. Gurbuz, and G. M. Rebeiz, "A 0.39–0.44 THz 2 × 4 amplifier-quadrupler array with peak EIRP of 3–4 dBm," *IEEE Trans. Microw. Theory Techn.*, vol. 61, no. 12, pp. 4483–4491, Dec. 2013.
[25] Y. Yang, O. D. Gurbuz, and G. M. Rebeiz, "An eight-element 370–410-GHz phased-array transmitter in 45-nm CMOS SOI with peak EIRP of 8–8.5 dBm," *IEEE Trans. Microw. Theory Techn.*, vol. 64, no. 12, pp. 4241–4249, Dec. 2016.
[26] T. Chi, M.-Y. Huang, S. Li, and H. Wang, "A packaged 90-to-300 GHz transmitter and 115-to-325 GHz coherent receiver in CMOS for full-band continuous-wave mm-wave hyperspectral imaging," in *IEEE Int. Solid-State Circuits Conf. (ISSCC) Dig. Tech. Papers*, vol. 60, Feb. 2017, pp. 304–305.
[27] E. Öjefors, J. Grzyb, Y. Zhao, B. Heinemann, B. Tillack, and U. R. Pfeiffer, "A 820 GHz SiGe chipset for terahertz active imaging applications," in *IEEE Int. Solid-State Circuits Conf. (ISSCC) Dig. Tech. Papers*, San Francisco, CA, USA, Feb. 2011, pp. 224–225.

[28] O. Momeni and E. Afshari, "High power terahertz and millimeter-wave oscillator design: A systematic approach," *IEEE J. Solid-State Circuits*, vol. 46, no. 3, pp. 583–597, Mar. 2011.

[29] R. Han and E. Afshari, "A CMOS high-power broadband 260-GHz radiator array for spectroscopy," *IEEE J. Solid-State Circuits*, vol. 48, no. 12, pp. 3090–3104, Dec. 2013.

[30] K. Sengupta and A. Hajimiri, "A 0.28 THz power-generation and beam-steering array in CMOS based on distributed active radiators," *IEEE J. Solid-State Circuits*, vol. 47, no. 12, pp. 3013–3031, Dec. 2012.

[31] R. Han *et al.*, "A SiGe terahertz heterodyne imaging transmitter with 3.3 mW radiated power and fully-integrated phase-locked loop," *IEEE J. Solid-State Circuits*, vol. 50, no. 12, pp. 2935–2947, Dec. 2015.

[32] G. Guimaraes and P. Reynaert, "A 660-to-676 GHz 4×2 oscillator-radiator array with intrinsic frequency-filtering feedback for harmonic power boost achieving 7.4 dBm EIRP in 40 nm CMOS," in *IEEE Int. Solid-State Circuits Conf. (ISSCC) Dig. Tech. Papers*, Feb. 2020, pp. 450–452.

[33] H. Saeidi, S. Venkatesh, C. R. Chappidi, T. Sharma, C. Zhu, and K. Sengupta, "A 4×4 distributed multi-layer oscillator network for harmonic injection and THz beamforming with 14 dBm EIRP at 416 GHz in a lensless 65 nm CMOS IC," in *IEEE Int. Solid-State Circuits Conf. (ISSCC) Dig. Tech. Papers*, Feb. 2020, pp. 256–258.

[34] Z. Hu, M. Kaynak, and R. Han, "High-power radiation at 1 THz in silicon: A fully scalable array using a multi-functional radiating mesh structure," *IEEE J. Solid-State Circuits*, vol. 53, no. 5, pp. 1313–1327, May 2018.

[35] K. Sengupta and A. Hajimiri, "A 0.28 THz 4×4 power-generation and beam-steering array," in *IEEE Int. Solid-State Circuits Conf. (ISSCC) Dig. Tech. Papers*, Feb. 2012, pp. 256–257.

[36] P. Hillger, J. Grzyb, R. Jain, and U. R. Pfeiffer, "Terahertz imaging and sensing applications with silicon-based technologies," *IEEE Trans. THz Sci. Technol.*, vol. 9, no. 1, pp. 1–19, Jan. 2019.

[37] K. Sengupta, T. Nagatsuma, and D. M. Mittleman, "Terahertz integrated electronic and hybrid electronic–photonic systems," *Nature Electron.*, vol. 1, no. 12, pp. 622–635, Dec. 2018.

[38] W. Knap *et al.*, "Plasma wave detection of sub-terahertz and terahertz radiation by silicon field-effect transistors," *Appl. Phys. Lett.*, vol. 85, no. 4, pp. 675–677, Jul. 2004.

[39] R. Tauk *et al.*, "Plasma wave detection of terahertz radiation by silicon field effects transistors: Responsivity and noise equivalent power," *Appl. Phys. Lett.*, vol. 89, no. 25, Dec. 2006, Art. no. 253511.

[40] E. Öjefors, U. R. Pfeiffer, A. Lisauskas, and H. G. Roskos, "A 0.65 THz focal-plane array in a quarter-micron CMOS process technology," *IEEE J. Solid-State Circuits*, vol. 44, no. 7, pp. 1968–1976, Jul. 2009.

[41] E. Öjefors, N. Baktash, Y. Zhao, R. A. Hadi, H. Sherry, and U. R. Pfeiffer, "Terahertz imaging detectors in a 65-nm CMOS SOI technology," in *Proc. IEEE Eur. Solid State Circuits Conf.*, Sep. 2010, pp. 486–489.

[42] H. Sherry *et al.*, "A 1kpixel CMOS camera chip for 25fps real-time terahertz imaging applications," in *IEEE Int. Solid-State Circuits Conf. (ISSCC) Dig. Tech. Papers*, Feb. 2012, pp. 252–253.

[43] S. Sankaran *et al.*, "Towards terahertz operation of CMOS," in *IEEE Int. Solid-State Circuits Conf. (ISSCC) Dig. Tech. Papers*, Feb. 2009, pp. 202–203.

[44] R. Han *et al.*, "A 280-GHz Schottky diode detector in 130-nm digital CMOS," *IEEE J. Solid-State Circuits*, vol. 46, no. 11, pp. 2602–2612, Nov. 2011.

[45] A. Tang and M.-C.-F. Chang, "Inter-modulated regenerative CMOS receivers operating at 349 and 495 GHz for THz imaging applications," *IEEE Trans. Terahertz Sci. Technol.*, vol. 3, no. 2, pp. 134–140, Mar. 2013.

[46] C. Jiang *et al.*, "A fully integrated 320 GHz coherent imaging transceiver in 130 nm SiGe BiCMOS," *IEEE J. Solid-State Circuits*, vol. 51, no. 11, pp. 2596–2609, Nov. 2016.

[47] C. Wang and R. Han, "Dual-terahertz-comb spectrometer on CMOS for rapid, wide-range gas detection with absolute specificity," *IEEE J. Solid-State Circuits*, vol. 52, no. 12, pp. 3361–3372, Dec. 2017.

[48] Q. Zhong, W. Choi, and K. O. Kenneth, "Terahertz even-order subharmonic mixer using symmetric MOS varactors," *IEEE J. Solid-State Circuits*, vol. 56, no. 2, pp. 355–366, Feb. 2021.

[49] D. Shim and K. O. Kenneth, "Symmetric varactor in 130-nm CMOS for frequency multiplier applications," *IEEE Electron Device Lett.*, vol. 32, no. 4, pp. 470–472, Apr. 2011.

[50] X. Yi, C. Wang, M. Lu, J. Wang, J. Grajal, and R. Han, "A terahertz FMCW comb radar in 65 nm CMOS with 100 GHz bandwidth," in *IEEE Int. Solid-State Circuits Conf. (ISSCC) Dig. Tech. Papers*, Feb. 2020, pp. 90–92.

[51] X. Yi, C. Wang, X. Chen, J. Wang, J. Grajal, and R. Han, "A 220-to-320-GHz FMCW radar in 65-nm CMOS using a frequency-comb architecture," *IEEE J. Solid-State Circuits*, vol. 56, no. 2, pp. 327–339, Feb. 2021.

[52] J. Al-Eryani, H. Knapp, J. Kammerer, K. Aufinger, H. Li, and L. Maurer, "Fully integrated single-chip 305–375-GHz transceiver with on-chip antennas in SiGe BiCMOS," *IEEE Trans. THz Sci. Technol.*, vol. 8, no. 3, pp. 329–339, May 2018.

[53] A. Mostajeran *et al.*, "A high-resolution 220-GHz ultra-wideband fully integrated ISAR imaging system," *IEEE Trans. Microw. Theory Techn.*, vol. 67, no. 1, pp. 329–339, 2019.

[54] B. P. Ginsburg, S. M. Ramaswamy, V. Rentala, E. Seok, S. Sankaran, and B. Haroun, "A 160 GHz pulsed radar transceiver in 65 nm CMOS," *IEEE J. Solid-State Circuits*, vol. 49, no. 4, pp. 984–995, Apr. 2014.

[55] A. Visweswaran *et al.*, "A 145 GHz FMCW-radar transceiver in 28 nm CMOS," in *IEEE Int. Solid-State Circuits Conf. (ISSCC) Dig. Tech. Papers*, Feb. 2019, pp. 168–170.

[56] T. Jaeschke, C. Bredendiek, and N. Pohl, "3D FMCW SAR imaging based on a 240 GHz SiGe transceiver chip with integrated antennas," in *Proc. 8th German Microw. Conf. (GeMiC)*, 2014, pp. 1–4.

[57] Z. Hu, C. Wang, and R. Han, "A 32-unit 240-GHz heterodyne receiver array in 65-nm CMOS with array-wide phase locking," *IEEE J. Solid-State Circuits*, vol. 54, no. 5, pp. 1216–1227, May 2019.

[58] K. Statnikov, J. Grzyb, B. Heinemann, and U. R. Pfeiffer, "160-GHz to 1-THz multi-color active imaging with a lens-coupled SiGe HBT chipset," *IEEE Trans. Microw. Theory Techn.*, vol. 63, no. 2, pp. 520–532, Feb. 2015.

[59] P. Hillger *et al.*, "A 128-pixel system-on-a-chip for real-time super-resolution terahertz near-field imaging," *IEEE J. Solid-State Circuits*, vol. 53, no. 12, pp. 3599–3612, Dec. 2018.

[60] C. Wang, B. Perkins, Z. Wang, and R. Han, "Molecular detection for unconcentrated gas with ppm sensitivity using 220-to-320-GHz dual-frequency-comb spectrometer in CMOS," *IEEE Trans. Biomed. Circuits Syst.*, vol. 12, no. 3, pp. 709–721, Jun. 2018.

[61] K.-E. Peiponen, A. Zeitler, and M. Kuwata-Gonokami, *Terahertz Spectroscopy and Imaging*. Berlin, Germany: Springer, 2012.

[62] C. H. Townes and A. L. Schawlow, *Microwave Spectroscopy*. New York, NY, USA: Dover, 2012.

[63] F. K. Tittel *et al.*, "Recent advances and applications of mid-infrared based trace gas sensor technology," *Proc. SPIE*, vol. 6900, Feb. 2008, Art. no. 69000Z.

[64] I. R. Medvedev *et al.*, "Analysis of exhaled human breath via terahertz molecular spectroscopy," in *Proc. 41st Int. Conf. Infr., Millim., THz Waves (IRMMW-THz)*, Sep. 2016, pp. 1–2.

[65] A. Amann *et al.*, "Analysis of exhaled breath for disease detection," *Annu. Rev. Anal. Chem.*, vol. 7, pp. 455–482, Jun. 2014.

[66] I. Medvedev, C. Neese, G. Plummer, and F. De Lucia, "Submillimeter spectroscopy for chemical analysis with absolute specificity," *Opt. Lett.*, vol. 35, no. 10, pp. 1533–1535, May 2010.

[67] K. Schmalz *et al.*, "245-GHz transmitter array in SiGe BiCMOS for gas spectroscopy," *IEEE Trans. THz Sci. Technol.*, vol. 6, no. 2, pp. 318–327, Mar. 2016.

[68] K. Schmalz, N. Rothbart, P. F.-X. Neumaier, J. Borngraber, H.-W. Hubers, and D. Kissinger, "Gas spectroscopy system for breath analysis at mm-wave/THz using SiGe BiCMOS circuits," *IEEE Trans. Microw. Theory Techn.*, vol. 65, no. 5, pp. 1807–1818, May 2017.

[69] N. Sharma *et al.*, "200–280 GHz CMOS RF front-end of transmitter for rotational spectroscopy," in *Dig. Tech. Papers, Symp. VLSI Technol.*, Jun. 2016, pp. 1–2.

[70] D. J. Nemchick, B. J. Drouin, A. J. Tang, Y. Kim, and M.-C.-F. Chang, "Sub-Doppler spectroscopy with a CMOS transmitter," *IEEE Trans. THz Sci. Technol.*, vol. 8, no. 1, pp. 121–126, Jan. 2018.

[71] A. Tang, B. Drouin, Y. Kim, G. Virbila, and M.-C.-F. Chang, "95–105 GHz 352 mW all-silicon cavity-coupled pulsed echo rotational spectroscopy system in 65 nm CMOS," *IEEE Trans. THz Sci. Technol.*, vol. 7, no. 3, pp. 244–249, May 2017.

[72] *Time and Phase Synchronization Aspects of Telecommunication Networks, Amendment 2*, ITU-T, Geneva, Switzerland, 2018.

[73] H. Li, L. Han, R. Duan, and G. M. Garner, "Analysis of the synchronization requirements of 5G and corresponding solutions," *IEEE Commun. Standards Mag.*, vol. 1, no. 1, pp. 52–58, Mar. 2017.

[74] L. Han *et al.*, "First national high-precision time synchronization network with sub-microsecond accuracy over commercial optical networks for wireless applications," in *Proc. Asia Commun. Photon. Conf. (ACP)*, Nov. 2014, pp. 1–3.

[75] A. T. Gardner and J. A. Collins, "Advancements in high-performance timing for long term underwater experiments: A comparison of chip scale atomic clocks to traditional microprocessor-compensated crystal oscillators," in *Proc. Oceans*, Oct. 2012, pp. 1–8.

[76] J. Vanier, "Atomic clocks based on coherent population trapping: A review," *Appl. Phys. B, Lasers Opt.*, vol. 81, no. 4, pp. 421–442, Aug. 2005.

[77] S. Knappe *et al.*, "A microfabricated atomic clock," *Appl. Phys. Lett.*, vol. 85, no. 9, pp. 1460–1462, Aug. 2004.

[78] D. Ruffieux, M. Contaldo, J. Haesler, and S. Lecomte, "A low-power fully integrated RF locked loop for miniature atomic clock," in *IEEE Int. Solid-State Circuits Conf. (ISSCC) Dig. Tech. Papers*, Feb. 2011, vol. 44, no. 1, pp. 48–49.

[79] Microsemi. *Microsemi SA.45s Chip Scale Atomic Clock Datasheet*. Accessed: Jan. 3, 2020. [Online]. Available: https://www.microsemi.com/product-directory

[80] H. Zhang *et al.*, "ULPAC: A miniaturized ultralow-power atomic clock," *IEEE J. Solid-State Circuits*, vol. 54, no. 11, pp. 3135–3148, Nov. 2019.

[81] R. Lutwak *et al.*, "The chip-scale atomic clock—Prototype evaluation," in *Proc. 39th Annu. Precise Time Time Interval Syst. Appl. Meeting (PTTI)*, 2007, pp. 269–290.

[82] C. Wang, X. Yi, M. Kim, Q. B. Yang, and R. Han, "A terahertz molecular clock on CMOS using high-harmonic-order interrogation of rotational transition for medium-/long-term stability enhancement," *IEEE J. Solid-State Circuits*, vol. 56, no. 2, pp. 566–580, Feb. 2021.

[83] C. Wang, X. Yi, J. Mawdsley, M. Kim, Z. Wang, and R. Han, "An on-chip fully electronic molecular clock based on sub-terahertz rotational spectroscopy," *Nature Electron.*, vol. 1, no. 7, pp. 421–427, Jul. 2018.

[84] M. Kim, C. Wang, Z. Hu, and R. Han, "Chip-scale terahertz carbonyl sulfide clock: An overview and recent studies on long-term frequency stability of OCS transitions," *IEEE Trans. THz Sci. Technol.*, vol. 9, no. 4, pp. 349–363, Jul. 2019.

[85] C. Wang *et al.*, "Chip-scale molecular clock," *IEEE J. Solid-State Circuits*, vol. 54, no. 4, pp. 914–926, Apr. 2019.

[86] T. Kürner, I. Kallfass, K. Ajito, A. Kasamatsu, D. Britz, and S. Priebe, *What's Next? Wireless Communication Beyond 60 GHz (Tutorial IG THz)*, document 15-12-0320-01-0thz, IEEE 802 Plenary Session, IEEE 802.15, San Diego, CA, USA, Jul. 2012.

[87] J. W. Holloway, G. C. Dogiamis, and R. Han, "A 105 Gb/s dielectric-waveguide link in 130 nm BiCMOS using channelized 220-to-335 GHz signal and integrated waveguide coupler," in *IEEE Int. Solid-State Circuits Conf. (ISSCC) Dig. Tech. Papers*, Feb. 2021, pp. 196–198.

[88] S. Fukuda *et al.*, "A 12.5+12.5 Gb/s full-duplex plastic waveguide interconnect," *IEEE J. Solid-State Circuits*, vol. 46, no. 12, pp. 3113–3125, Dec. 2011.

[89] N. Van Thienen, Y. Zhang, M. De Wit, and P. Reynaert, "An 18 Gbps polymer microwave fiber (PMF) communication link in 40 nm CMOS," in *Proc. Eur. Solid-State Circuits Conf.*, Lausanne, Switzerland, Sep. 2016, pp. 483–486.

[90] M. De Wit, Y. Zhang, and P. Reynaert, "Analysis and design of a foam-cladded PMF link with phase tuning in 28-nm CMOS," *IEEE J. Solid-State Circuits*, vol. 54, no. 7, pp. 1960–1969, Jul. 2019.

[91] Q. J. Gu, "Sub-THz/THz interconnect, complement to electrical and optical interconnects: Addressing fundamental challenges related to communication distances," *IEEE Solid State Circuits Mag.*, vol. 12, no. 4, pp. 20–32, Fall 2020.

[92] M. Sawaby, N. Dolatsha, B. Grave, C. Chen, and A. Arbabian, "A fully packaged 130-GHz QPSK transmitter with an integrated PRBS generator," *IEEE Solid-State Circuits Lett.*, vol. 1, no. 7, pp. 166–169, Jul. 2018.

[93] J. W. Holloway, G. C. Dogiamis, and R. Han, "Innovations in terahertz interconnects: High-speed data transport over fully electrical terahertz waveguide links," *IEEE Microw. Mag.*, vol. 21, no. 1, pp. 35–50, Jan. 2020.

[94] J. W. Holloway, L. Boglione, T. M. Hancock, and R. Han, "A fully integrated broadband sub-mmWave chip-to-chip interconnect," *IEEE Trans. Microw. Theory Techn.*, vol. 65, no. 7, pp. 2373–2386, Jul. 2017.

[95] S. Dang, O. Amin, B. Shihada, and M.-S. Alouini, "What should 6G be?" *Nature Electron.*, vol. 3, no. 1, pp. 20–29, Jan. 2020.

[96] T. S. Rappaport *et al.*, "Wireless communications and applications above 100 GHz: Opportunities and challenges for 6G and beyond," *IEEE Access*, vol. 7, pp. 78729–78757, 2019.

[97] M. Polese, J. M. Jornet, T. Melodia, and M. Zorzi, "Toward end-to-end, full-stack 6G terahertz networks," *IEEE Commun. Mag.*, vol. 58, no. 11, pp. 48–54, Nov. 2020.

[98] V. Petrov, T. Kurner, and I. Hosako, "IEEE 802.15.3d: First standardization efforts for sub-terahertz band communications toward 6G," *IEEE Commun. Mag.*, vol. 58, no. 11, pp. 28–33, Nov. 2020.

[99] (2019). *Federal Communication Commission (FCC) Takes Steps to Open Spectrum Horizons for New Services and Technologies*. [Online]. Available: https://docs.fcc.gov/public/attachments/DOC-356588A1.pdf

[100] Z. Wang, P.-Y. Chiang, P. Nazari, C.-C. Wang, Z. Chen, and P. Heydari, "A 210 GHz fully integrated differential transceiver with fundamental-frequency VCO in 32 nm SOI CMOS," in *IEEE Int. Solid-State Circuits Conf. (ISSCC) Dig. Tech. Papers*, Feb. 2013, pp. 136–137.

[101] J.-D. Park, S. Kang, S. V. Thyagarajan, E. Alon, and A. M. Niknejad, "A 260 GHz fully integrated CMOS transceiver for wireless chip-to-chip communication," in *IEEE Symp. VLSI Circuits, Dig. Tech. Papers*, Jun. 2012, pp. 48–49.

[102] D. Fritsche, P. Starke, C. Carta, and F. Ellinger, "A low-power SiGe BiCMOS 190-GHz transceiver chipset with demonstrated data rates up to 50 Gbit/s using on-chip antennas," *IEEE Trans. Microw. Theory Techn.*, vol. 65, no. 9, pp. 3312–3323, Sep. 2017.

[103] P. Rodriguez-Vazquez, J. Grzyb, N. Sarmah, B. Heinemann, and U. R. Pfeiffer, "A 65 Gbps QPSK one meter wireless link operating at a 225–255 GHz tunable carrier in a SiGe HBT technology," in *Proc. IEEE Radio Wireless Symp. (RWS)*, Jan. 2018, pp. 146–149.

[104] P. Rodriguez-Vazquez, J. Grzyb, B. Heinemann, and U. R. Pfeiffer, "A 16-QAM 100-Gb/s 1-M wireless link with an EVM of 17% at 230 GHz in an SiGe technology," *IEEE Microw. Wireless Compon. Lett.*, vol. 29, no. 4, pp. 297–299, Apr. 2019.

[105] S. Lee *et al.*, "An 80-Gb/s 300-GHz-band single-chip CMOS transceiver," *IEEE J. Solid-State Circuits*, vol. 54, no. 12, pp. 3577–3588, Dec. 2019.

[106] P. Rodriguez-Vazquez, J. Grzyb, B. Heinemann, and U. R. Pfeiffer, "A QPSK 110-Gb/s polarization-diversity MIMO wireless link with a 220–255 GHz tunable LO in a SiGe HBT technology," *IEEE Trans. Microw. Theory Techn.*, vol. 68, no. 9, pp. 3834–3851, Sep. 2020.

[107] M. I. W. Khan *et al.*, "CMOS THz-ID: A 1.6-mm^2 package-less identification tag using asymmetric cryptography and 260-GHz far-field backscatter communication," *IEEE J. Solid-State Circuits*, vol. 56, no. 2, pp. 340–354, Feb. 2021.

[108] R. Want, "An introduction to RFID technology," *IEEE Pervasive Comput.*, vol. 5, no. 1, pp. 25–33, Jan./Mar. 2006.

[109] M. I. Ibrahim *et al.*, "THzID: A 1.6 mm^2 package-less cryptographic identification tag with backscattering and beam-steering at 260 GHz," in *IEEE Int. Solid-State Circuits Conf. (ISSCC) Dig. Tech. Papers*, Feb. 2020, pp. 454–455.

[110] J. Hermans, R. Peeters, and C. Onete, "Efficient, secure, private distance bounding without key updates," in *Proc. 6th ACM Conf. Secur. Privacy Wireless Mobile Netw.*, 2013, pp. 207–218.

[111] H.-J. Song, "Packages for terahertz electronics," *Proc. IEEE*, vol. 105, no. 6, pp. 1121–1138, Jun. 2017.

[112] J.-Y. Kim, H.-Y. Lee, J.-H. Lee, and D.-P. Chang, "Wideband characterization of multiple bondwires for millimeter-wave applications," in *Proc. Asia–Pacific Microw. Conf. (APMC)*, 2000, pp. 1265–1268.

[113] W. Deal, X. B. Mei, K. M. K. H. Leong, V. Radisic, S. Sarkozy, and R. Lai, "THz monolithic integrated circuits using InP high electron mobility transistors," *IEEE Trans. THz Sci. Technol.*, vol. 1, no. 1, pp. 25–32, Sep. 2011.

[114] R. Han *et al.*, "Active terahertz imaging using Schottky diodes in CMOS: Array and 860-GHz pixel," *IEEE J. Solid-State Circuits*, vol. 48, no. 10, pp. 2296–2308, Oct. 2013.

[115] J. W. Holloway, G. C. Dogiamis, S. Shin, and R. Han, "220-to-330-GHz manifold triplexer with wide stopband utilizing ridged substrate integrated waveguides," *IEEE Trans. Microw. Theory Techn.*, vol. 68, no. 8, pp. 3428–3438, Aug. 2020.

[116] A. Aleksov *et al.*, "Organic package substrates using lithographic via technology for RF to THz applications," in *IEDM Tech. Dig.*, Dec. 2020, pp. 17.5.1–17.5.4.

[117] N. Deferm and P. Reynaert, "A 120 GHz fully integrated 10 Gb/s short-range star-QAM wireless transmitter with on-chip bondwire antenna in 45 nm low power CMOS," *IEEE J. Solid-State Circuits*, vol. 49, no. 7, pp. 1606–1616, Jul. 2014.

[118] A. Bisognin *et al.*, "Ball grid array module with integrated shaped lens for 5G backhaul/fronthaul communications in F-band," *IEEE Trans. Antennas Propag.*, vol. 65, no. 12, pp. 6380–6394, Dec. 2017.